A cryptic tubulin-binding domain links MEKK1 to curved tubulin protomers

Pavel Filipčík[a], Sharissa L. Latham[b,c], Antonia L. Cadell[b], Catherine L. Day[a], David R. Croucher[b,c], and Peter D. Mace[a,1]

[a]Biochemistry Department, School of Biomedical Sciences, University of Otago, 9054 Dunedin, New Zealand; [b]The Kinghorn Cancer Centre, Garvan Institute of Medical Research, Sydney, NSW 2010, Australia; and [c]St Vincent's Hospital Clinical School, University of New South Wales, Sydney, NSW 2052, Australia

Edited by Melanie H. Cobb, University of Texas Southwestern Medical Center, Dallas, TX, and approved July 27, 2020 (received for review April 7, 2020)

The MEKK1 protein is a pivotal kinase activator of responses to cellular stress. Activation of MEKK1 can trigger various responses, including mitogen-activated protein (MAP) kinases, NF-κB signaling, or cell migration. Notably, MEKK1 activity is triggered by microtubule-targeting chemotherapies, among other stressors. Here we show that MEKK1 contains a previously unidentified tumor overexpressed gene (TOG) domain. The MEKK1 TOG domain binds to tubulin heterodimers—a canonical function of TOG domains—but is unusual in that it appears alone rather than as part of a multi-TOG array, and has structural features distinct from previously characterized TOG domains. MEKK1 TOG demonstrates a clear preference for binding curved tubulin heterodimers, which exist in soluble tubulin and at sites of microtubule polymerization and depolymerization. Mutations disrupting tubulin binding decrease microtubule density at the leading edge of polarized cells, suggesting that tubulin binding may play a role in MEKK1 activity at the cellular periphery. We also show that MEKK1 mutations at the tubulin-binding interface of the TOG domain recur in patient-derived tumor sequences, suggesting selective enrichment of tumor cells with disrupted MEKK1–microtubule association. Together, these findings provide a direct link between the MEKK1 protein and tubulin, which is likely to be relevant to cancer cell migration and response to microtubule-modulating therapies.

MAPK | kinase | MEKK1 | tubulin

Mitogen-activated protein kinase (MAPK) signaling is used throughout eukaryotic organisms as a means of regulating proliferation, differentiation, and stress responses. In general, MAPK signaling occurs via hierarchical cascades, where a MAPK is activated following phosphorylation by a MAP kinase kinase (MAP2K), which itself is activated by a MAP kinase kinase kinase (MAP3K). The molecular basis of regulation of MAPKs and MAP2Ks is relatively well established (1). However, the diversity inherent to the 24 MAP3Ks present in humans means that, outside of a few well-studied cases, most notably RAF kinases (2–4), the molecular mechanisms underlying MAP3K regulation remain relatively poorly understood.

MEKK1 (also known as MAP3K1) is unique in that it is the only MAP3K to also possess ubiquitin E3 ligase activity. The ability to phosphorylate or ubiquitinate substrates under different circumstances allows MEKK1 to function as a central signaling hub—it can promote signaling via the ERK, JNK, p38, NF-κB, or other pathways, depending on cellular context (5–8). Direct targets for MEKK1 kinase activity include MAP2Ks, leading to activation of JNK, ERK, and p38 pathways; inhibitor of κ kinases (IκKs), leading to NF-κB transcription factor family activation (6, 9, 10); or migration-linked proteins such as calponin-3 (11). MEKK1 can ubiquitinate itself in a phosphorylation-dependent manner (12), leading to attenuation of its own kinase activity, and the diminished activity of downstream ERK and JNK pathways. Alternatively, ubiquitination of MEKK1 can increase its kinase activity upon CD40 stimulation (13). MEKK1 can also ubiquitinate TAB1 with K63-linked polyubiquitin chains, leading to p38, JNK, and TAK1 activation (14). MEKK1 is also involved in the control of ERK and c-Jun stability via K48-linked polyubiquitination and proteasomal degradation (15–17).

Activation of MEKK1 can result in many cellular outcomes, ranging from proliferation to apoptosis, depending on cellular context. It is therefore necessary to control its activation both temporally and spatially in order to ensure robust, specific responses to given stimuli. MEKK1 is associated with many subcellular structures, including tight junctions (18), actin stress fibers, focal adhesions (19), the cytoplasmic membrane (13, 20), and the perinuclear region (15).

In terms of domain architecture, MEKK1 contains N-terminal SWIM-type and RING-type zinc finger domains, and a C-terminal serine–threonine kinase domain (Fig. 1*A*). The SWIM domain is thought to mediate protein–protein interactions and bind c-Jun, while the RING domain exerts ubiquitin E3 ligase activity (14, 16, 21). MEKK1 also contains a caspase-3 cleavage site at Asp-878 that, when cleaved, separates the kinase domain from the SWIM and RING domains (22–24). Aside from recruitment to α-actinin and stress fibers via a region incorporating the SWIM–RING domains (19), little is known about the factors that regulate MEKK1 localization, and thus signaling outcome.

Here, we show that MEKK1 contains a cryptic tumor overexpressed gene (TOG) domain, which allows it to bind directly to tubulin. A crystal structure of the MEKK1 TOG domain reveals differences from canonical TOG domains in the α-tubulin binding surface. The MEKK1 TOG domain shows a clear preference for binding to the curved conformation of tubulin, which

Significance

The protein kinase MEKK1 activates stress-signaling pathways in response to various cellular stressors, including chemotherapies that disrupt dynamics of the tubulin cytoskeleton. We show that MEKK1 contains a previously uncharacterized domain that can preferentially bind to the curved tubulin heterodimer—which is found in soluble tubulin and at sites of microtubule assembly and disassembly. Mutations that interfere with MEKK1–tubulin binding disrupt microtubule networks in migrating cells and are enriched in patient-derived tumor sequences. These results suggest that MEKK1–tubulin binding may be relevant to cancer progression, and the efficacy of microtubule-disrupting chemotherapies that require the activity of MEKK1.

Author contributions: P.F., S.L.L., C.L.D., D.R.C., and P.D.M. designed research; P.F., S.L.L., and A.L.C. performed research; P.F., S.L.L., C.L.D., D.R.C., and P.D.M. analyzed data; and P.F. and P.D.M. wrote the paper.

The authors declare no competing interest.

This article is a PNAS Direct Submission.

This open access article is distributed under Creative Commons Attribution-NonCommercial-NoDerivatives License 4.0 (CC BY-NC-ND).

[1]To whom correspondence may be addressed. Email: peter.mace@otago.ac.nz.

This article contains supporting information online at https://www.pnas.org/lookup/suppl/doi:10.1073/pnas.2006429117/-/DCSupplemental.

First published August 17, 2020.

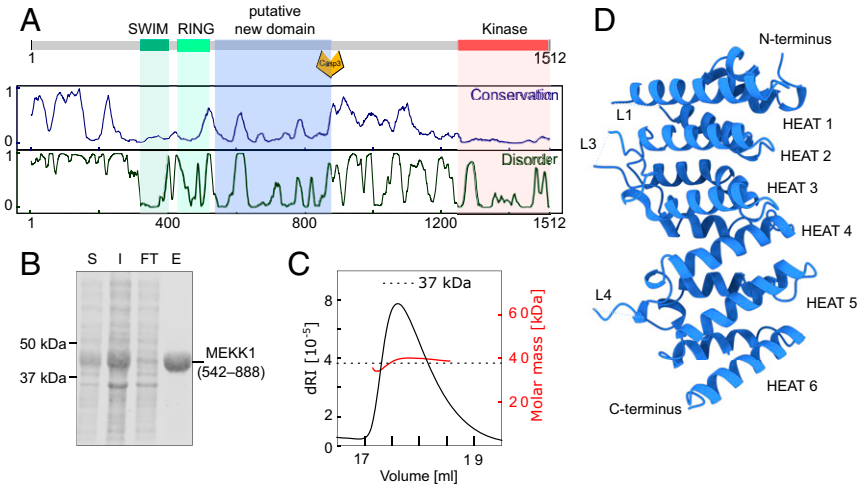

Fig. 1. Identification and structure of an uncharacterized domain of MEKK1. (*A*) Analysis of MEKK1 sequence conservation across species and predicted disorder. *Top* shows a schematic representation of known features of MEKK1, relative to sequence conservation (*Middle*) and predicted disorder (*Bottom*). (*B*) MEKK1(542 to 888) can be expressed and purified from *E. coli*. S, I, FT, and E indicate soluble (S), insoluble (I), flow-through (FT), and eluate (E) fractions from lysis and Ni^{2+} affinity purification, as visualized using Coomassie staining. (*C*) MALLS analysis of MEKK1(542 to 888) indicates a monomeric species in solution. (*D*) The crystal structure of MEKK1(548 to 867), with termini and structural features labeled. Missing loops are denoted with L1, L3 and L4.

is adopted by soluble tubulin and at dynamic microtubule ends. Disrupting the tubulin-binding surface reduces microtubule density at the leading edge of polarized cells, and has the potential to link microtubule dynamics to MEKK1 activity in chemotherapeutic response.

Results

A Previously Unidentified Domain within MEKK1. Since its discovery, MEKK1 has been annotated as containing SWIM, RING, and kinase domains (10, 15, 16). To gain further insight into the molecular basis for MEKK1 regulation, we combined analysis of sequence conservation across species and prediction of protein disorder (Fig. 1*A*). From this analysis, we observed that a large portion of MEKK1, between the RING domain and the caspase cleavage site, is highly conserved and displays characteristics consistent with the presence of a structured domain. Notably, MEKK1 from diverse metazoans has a conserved region from Asn540 to Gly872 (human numbering), and PONDr (25) analysis of the sequence suggested a well-ordered domain (Fig. 1*A* and *SI Appendix*, Fig. S1). Because this region had not previously been functionally annotated, we cloned residues 542 to 888 of human MEKK1 to investigate its function.

Following overexpression of His-tagged protein in *Escherichia coli* (Fig. 1*B*), we observed that MEKK1(542 to 888) eluted as a monodisperse peak upon size-exclusion chromatography (SEC). Analysis using SEC coupled to multiangle laser light scattering (SEC-MALLS) confirmed that the domain was monomeric and that it did not form aggregates in solution (Fig. 1*C*). We grew crystals of MEKK1(542 to 888), solved its structure using experimental phasing (Fig. 1*D* and *SI Appendix*, Fig. S2), and refined the final structure against native diffraction data to a resolution of 1.9 Å (*SI Appendix*, Table S1).

MEKK1 Contains a Cryptic TOG Domain. The structure of MEKK1(542 to 888) consists of six helix–loop–helix repeats side by side in an extended array (Fig. 1*D*). Such helix–loop–helix repeats are designated as HEAT (Huntingtin, Elongation factor 3, protein phosphatase 2A, and yeast kinase TOR1) repeats. The loops connecting the helical array showed notable differences in character on either side of the molecule; on one side, the loops are compact, well defined by electron density, and conserved in MEKK1 from various organisms, while, on the opposing side of the molecule, the loops (L1, L3, and L4) are longer, poorly defined by electron density, and less well conserved in sequence (*SI Appendix*, Fig. S3). To assess similarity to known functional domains, we searched for similar structures using the PDBeFold server (26), which uncovered remarkable similarity to structures of TOG domains from human, mouse, and *Drosophila* (*SI Appendix*, Table S2). While TOG domain primary sequences are quite divergent (*SI Appendix*, Figs. S3 and S4), TOG domains generally adopt a similar fold with six HEAT repeats, with some variation at the N and C termini. Based on this observed structural similarity, we subsequently refer to the region covering residues 548 to 867 of MEKK1 as the MEKK1 TOG domain.

The primary role of TOG domains is to mediate direct interaction with tubulin and/or microtubules, which raised the possibility that MEKK1 may bind directly to tubulin. A direct MEKK1–tubulin interaction was particularly intriguing in light of previous evidence that MEKK1 responds to microtubule stress in a manner distinct from its response to other stressors (23, 27–29). The canonical function of TOG domains is the regulation of microtubule dynamics through conformation-specific binding to tubulin (30–33). MEKK1 only contains one TOG domain, and, while TOG domains often occur in arrays, recent work has shown that even isolated TOG domains can modulate microtubule dynamics (34, 35). We therefore set out to ascertain whether the MEKK1 TOG domain does, in fact, bind to tubulin, and, secondly, whether binding may be sensitive to tubulin conformation—namely, whether it preferentially binds the curved tubulin heterodimer or intact (straight) microtubules.

Model of an MEKK1–Tubulin Interaction. In order to better visualize the similarities and differences between the MEKK1 TOG domain and TOG domains that recognize various states of tubulin, a set of models was prepared (30, 31, 36, 37). These models allowed direct comparison of the features that drive the conformational preference of different TOG domains relative to the MEKK1 TOG domain (Fig. 2). The structures of *Saccharomyces cerevisiae* Stu2p TOG1 and *Drosophila melanogaster* Msps TOG5 were used for this comparison because they preferentially bind curved and straight tubulin, respectively. The MEKK1 TOG-Stu2p TOG1 alignment has a Cα rmsd of 3.84 Å over 185 aligned residues with 13% sequence identity (Fig. 2*A* and *SI Appendix*, Table S3), and the MEKK1 TOG-Msps TOG5 has a Cα rmsd of 3.16 Å over 193 aligned residues with 11.4% sequence identity (Fig. 2*C* and *SI Appendix*,

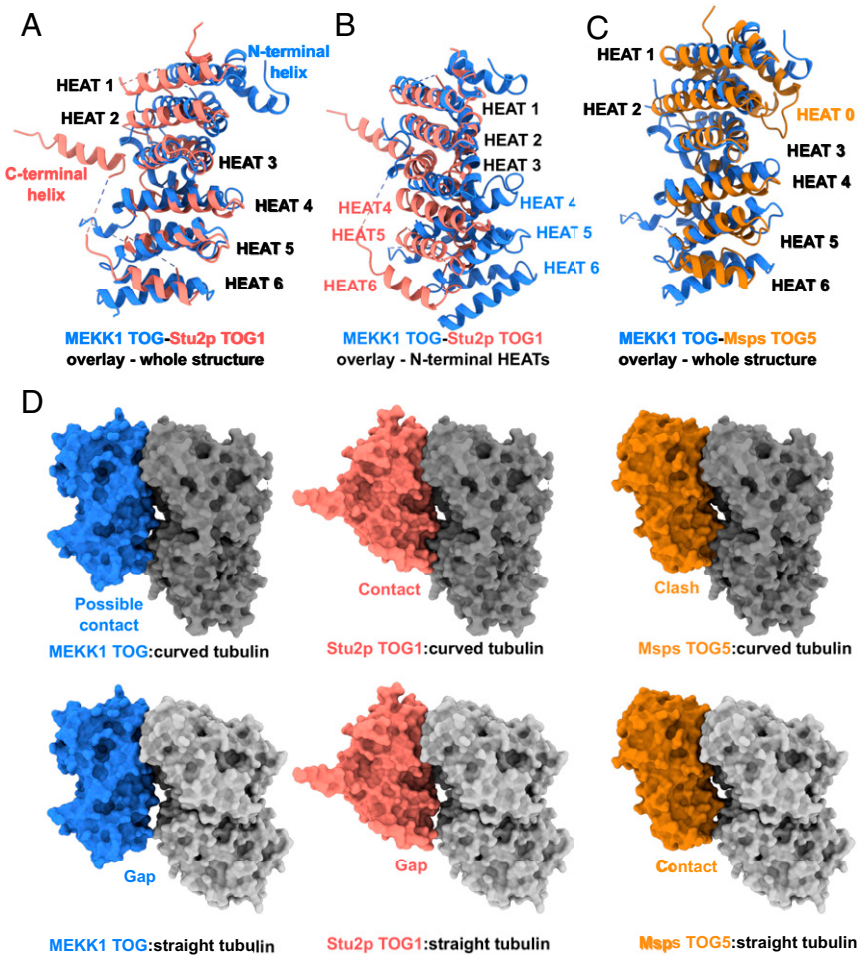

Fig. 2. Comparison of TOG domains and their tubulin-binding modes: (*A*) MEKK1 TOG domain (blue, PDB ID code 6WHB) superimposed on Stu2p TOG1 domain (salmon, PDB ID code 4FFB) using secondary structure alignment across the whole structure. MEKK1 contains an additional structured helix on its N terminus (labeled in blue), while Stu2p TOG1's C-terminal helix (labeled in salmon) is found in a different position. (*B*) Secondary structure superimposition of MEKK1 TOG and Stu2p TOG1, using only the N-terminal three HEAT repeats for alignment. This alignment showcases the difference in angle between HEAT 3 and HEAT 4 in Stu2p and MEKK1, leading to diverging orientation of the following HEAT repeats. (*C*) MEKK1 TOG domain (blue) superimposed on Msps TOG5 domain (orange, PDB ID code 5VJC) using secondary structure alignment across the whole structure. Msps TOG5 contains an additional HEAT 0 repeat (labeled in orange) on its N terminus. (*D*) Surface representations of MEKK1 TOG (blue), Stu2p TOG1 (salmon), and Msps TOG5 (orange) models shown in *A* and *C* in complex with (*Top*) curved tubulin (dark gray, PDB ID code 4FFB) and (*Bottom*) straight tubulin (light gray, PDB ID code 5SYF) showcases the differences in the extent and quality of contacts between the respective TOG domains and the α-tubulin subunit.

Table S3). Overlaying the three N-terminal HEAT repeats of MEKK1 TOG onto Stu2p leads to a better fit, but to a large displacement of the three C-terminal HEAT repeats due to the different relative arrangement of the repeats (Fig. 2*B*). Overall, the TOG domain in MEKK1 has strong structural conservation in the core HEAT repeat array with TOG domains that bind either straight or curved tubulin. The main differences between the domains lies in their N and C termini, and in the relative orientation of successive HEAT repeats (Fig. 2 *A*–*C*).

Next, we considered the potential of the MEKK1 TOG domain to bind the curved (Fig. 2 *D*, *Top*) or straight (Fig. 2 *D*, *Bottom*) forms of tubulin. The MEKK1 TOG shows electrostatic properties complementary to tubulin across the putative interface (*SI Appendix*, Fig. S5). When compared to Stu2p, which binds curved tubulin, MEKK1 TOG contains a full C-terminal HEAT repeat where Stu2p has only a single helix (Fig. 2*A*). MEKK1 TOG's additional helix within HEAT 6 is arginine rich, a feature shared with only one other structurally characterized TOG domain, Cep104 TOG (*SI Appendix*, Fig. S6). Compared to a straight tubulin binding TOG5 in Msps, MEKK1 TOG has a single helix at its N terminus, whereas Msps has a pair of helices known as HEAT 0 (Fig. 2*C*). HEAT 0 is thought to facilitate microtubule binding by contacting an adjacent protofilament in the microtubule lattice. The overlays alone do not clearly suggest a tubulin preference for the MEKK1—largely because the arrangement of HEAT repeats in the MEKK1 TOG is somewhat divergent. Superimposing all or some of the HEAT repeats gives quite different models (Fig. 2 *A* and *B*) making it difficult to conclusively assess the putative tubulin interface (Fig. 2*D*). Thus, it appears that the MEKK1 TOG domain bears similarities to both curved tubulin-binding TOGs and lattice-binding TOGs (Fig. 2 *A* and *C*), but it is not readily apparent precisely which conformation of tubulin it may prefer.

MEKK1 Binds Tubulin in Solution. To investigate whether the TOG domain of MEKK1 is capable of tubulin binding, we first tested its ability to bind tubulin in vitro using SEC coelution assays with soluble αβ-tubulin. These assays showed that MEKK1 TOG is able to bind free soluble tubulin (Fig. 3 *A* and *B*), with TOG domain coeluting together with tubulin in the front peak at a higher apparent molecular weight than tubulin alone. Although this demonstrated that the TOG domain can bind the isolated tubulin heterodimer, tubulin can adopt a continuum of conformations

in solution (38), so we also evaluated binding to a specific curved conformation of tubulin, stabilized with colchicine (38–40). Using the same assay, we observed that colchicine-stabilized tubulin was still able to form a higher molecular weight complex with the MEKK1 TOG, although slightly less effectively (Fig. 3*C* and *SI Appendix*, Fig. S7). Together, these experiments showed that MEKK1 TOG domain is a bona fide TOG domain, and suggested that MEKK1 TOG can bind the curved conformation of tubulin.

We next probed the contribution of different regions of the MEKK1 TOG domain to binding. Although divergent in sequence overall, the β-tubulin contacting residues in Stu2p TOG1 are conserved in MEKK1 TOG (Fig. 3 *D*–*F*). The arginine-rich C-terminal helix of MEKK1 TOG is positioned in the vicinity of the acidic α-tubulin residues, suggesting an extended α-tubulin interaction surface in MEKK1 TOG (Fig. 3 *G* and *H* and *SI Appendix*, Fig. S5). Thus, we designed mutants at each interface: the β-tubulin interacting Trp-577 and Val-647 patch (Fig. 3*F*), and the C-terminal arginine-rich helix of MEKK1 TOG, which significantly differs from the C-terminal helices of Stu2p (Fig. 3 *G* and *H*).

Tubulin coelution assays with MEKK1 TOG mutants showed that both α- and β-tubulin interfaces are involved in the interaction between TOG and tubulin (Fig. 3*I* and *SI Appendix*, Fig. S7). On the β-tubulin–interacting side, the Val-647-Asp mutant disrupted tubulin coelution completely (Fig. 3*I* and *SI Appendix*, Fig. S7). The importance of the unique arginine-rich C-terminal HEAT repeat of MEKK1 for tubulin binding was probed with a charge swap mutation of Arg-851, situated at the head of the arginine-rich C-terminal helix of MEKK1 TOG (R851E; Fig. 3*H*). The Arg-851-Glu mutant disrupted interaction with tubulin to the same extent as a Val-647-Asp mutation in the β-tubulin interface (Fig. 3*I* and *SI Appendix*, Fig. S7).

These results show that MEKK1 TOG can bind the curved conformation of soluble tubulin, and that both of the interfaces implicated by modeling (Figs. 2 and 3) are important for the MEKK1 TOG:tubulin interaction.

Analysis of Conformation-Specific Binding by MEKK1 TOG. As TOG domains can bind tubulin in a conformation-specific manner (30–33), it was necessary to probe whether the unusual features

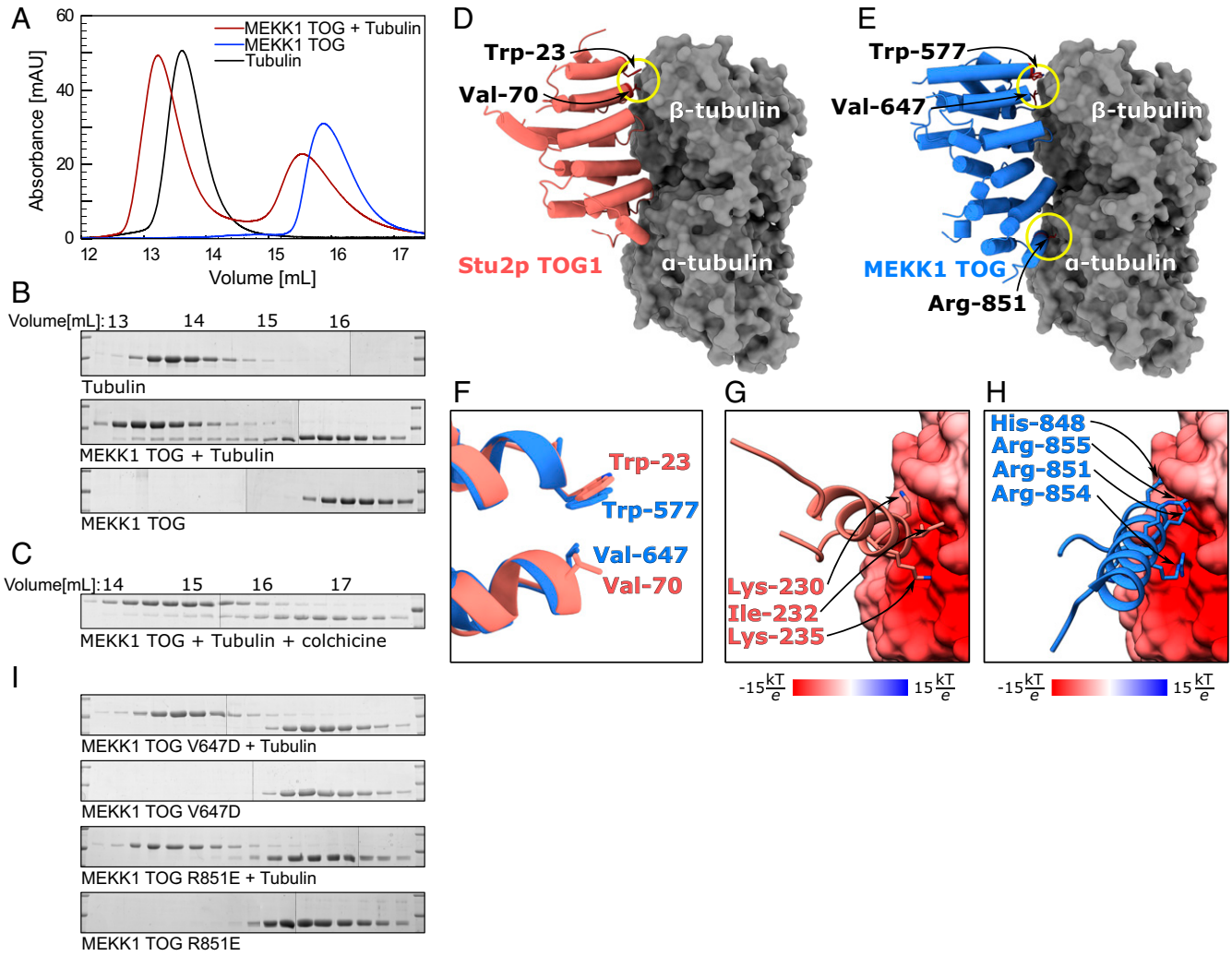

Fig. 3. Tubulin binding and mutation analysis of MEKK1 TOG. (*A*) SEC trace of MEKK1 TOG (blue), tubulin (black), and their combination (red). Earlier elution of TOG and tubulin in combination suggests binding interaction. (*B*) SDS/PAGE analyses of SEC coelution experiments of MEKK1 TOG with tubulin. (*C*) SDS/PAGE analysis of SEC coelution assay with MEKK1 TOG and colchicine-treated tubulin. (*D*) The crystal structure of Stu2p TOG1–tubulin complex, used as the basis for mutant design. (*E*) A model of MEKK1 TOG interacting with tubulin, highlighting the conserved residues Trp-577 and Val-647, as well as the C-terminal Arg-851, tested in this work. (*F*) A detail of the β-tubulin interface, conserved between Stu2p TOG, and MEKK1. (*G* and *H*) Details of the C-terminal portions of Stu2p TOG and MEKK1 TOG, respectively, with tubulin surface colored by electrostatic potential. (*I*) SDS/PAGE analyses of SEC coelution experiments of MEKK1 TOG mutants with tubulin.

of the MEKK1 TOG may enable it to recognize straight as well as curved tubulin. We probed the ability of MEKK1 TOG to bind to the straight conformation of tubulin in the microtubule lattice using paclitaxel-stabilized microtubules in cosedimentation assays (*SI Appendix*, Fig. S8 *A* and *B*), negative stain electron microscopy (NS-EM) (*SI Appendix*, Fig. S8 *C* and *D*), and cryo-EM (*SI Appendix*, Fig. S8 *E* and *F*). In cosedimentation assays, a greater proportion of MEKK1 TOG was found in the insoluble fraction cosedimented with paclitaxel-stabilized microtubules than in control experiments lacking microtubules (*SI Appendix*, Fig. S8 *A* and *B*). The presence of MEKK1 TOG in the insoluble fraction suggested that interaction with the straight conformation of tubulin may be possible, so this was probed further by EM. Although NS-EM suggested density on the outside of the microtubule lattice with regular spacings (*SI Appendix*, Fig. S8 *C* and *D*), MEKK1 TOG binding to paclitaxel-stabilized microtubules was not apparent by cryo-EM. No densities consistent with a microtubule-binding protein were apparent in raw micrographs of microtubules in the presence of MEKK1 TOG (*SI Appendix*, Fig. S8*E*), and two-dimensional (2D) class averages of helix particles from the cryo-EM preparation show no classes with regularly spaced densities decorating the outside of the microtubule (*SI Appendix*, Fig. S8*F*).

With cosedimentation assays and EM studies proving equivocal, we turned to isothermal titration calorimetry (ITC) to test for conformation specific binding. ITC made it possible to test binding to the free and polymerized, paclitaxel-stabilized form of tubulin directly, using the same experimental conditions in both cases. A global analysis of the thermograms of four independent experiments with free tubulin (Fig. 4*A*, shown in blue, maroon, yellow, and orange) clearly shows 1:1 stoichiometric binding with a calculated dissociation constant K_D = 0.63 μM in 250 mM NaCl, 250 μM tris(2-carboxyethyl)phosphine (TCEP), 10 μM guanosine triphosphate (GTP), and 20 mM sodium phosphate pH 6.5. The titrations contained relatively high salt to maintain stability of the MEKK1 TOG domain. Thus, the MEKK1–tubulin complex dissociation constant may be even lower in more permissive conditions. The control titrations of TOG into buffer and buffer into tubulin (Fig. 4*A*, both shown in cyan) both show negligible contributions of the dilution effects. No interaction was detectable upon injection of MEKK1 TOG domain into paclitaxel-stabilized microtubules (Fig. 4*B*, shown in blue and maroon).

Thus, the TOG domain of MEKK1 shows clear preference in binding to the nonpolymerized form of tubulin, as opposed to polymerized, paclitaxel-stabilized microtubules. The nonpolymerized (curved) form of the tubulin heterodimer is also found at polymerizing and depolymerizing microtubule ends (41, 42), suggesting that the MEKK1 TOG domain may bind tubulin at these sites, in addition to the nonpolymerized form of tubulin.

TOG–Tubulin Binding Impacts Leading-Edge Tubulin in Polarized Cells. We next investigated how the binding preference for curved tubulin influenced MEKK1 localization in cells. We visualized the cellular localization of wild-type (WT) MEKK1 and a double mutant incorporating two disruptive mutants at the tubulin-binding interface (V647D/R851E). In general, both the WT and mutant MEKK1 are observed throughout the cell, but are enriched at the cytoplasmic membrane (Fig. 5*A*). Remarkably, microtubule density at the cellular periphery visualized by tubulin staining appeared to be reduced in mutant-transfected cells (Fig. 5*B*). To quantify this effect, we analyzed cells within a scratch assay in order to induce a clear polarized morphology, where the nucleus was positioned toward the rear of the cell and the centrosomes were repositioned toward the cell's leading edge. The leading edge was manually demarcated using the MEKK1 signal, and the coverage of microtubules within a 15-pixel region of interest (ROI) from the leading edge was quantified (Fig. 5*C*). In this analysis, coverage of microtubules at the leading edge is significantly reduced in the presence of the MEKK1 V647D/R851E mutant compared to the WT (Fig. 5*D*). The effect was independent of the size of the leading-edge region analyzed (*SI Appendix*, Fig. S9*A*), and the expression levels of MEKK1 were not significantly different between the WT and V647D/R851E mutant (*SI Appendix*, Fig. S9*B*). Thus, disrupted tubulin binding by MEKK1 appears to result in less microtubule penetration at the migrating leading edge. This observation could be consistent with either regulation of MEKK1 by enrichment at the plus end of polymerizing and depolymerizing tubulin or MEKK1 binding free tubulin heterodimers in solution to interfere with microtubule dynamics at the leading edge.

MEKK1–Tubulin Interface Mutants Are Enriched in Tumor Samples. Having observed MEKK1 at the leading edge of cells, and with prior studies showing MEKK1 is required for efficacy of antimicrotubule chemotherapies, we considered how tubulin binding may impact cancer spread or therapy. Mutations in MEKK1 occur at elevated rates in breast and other cancer types (43, 44), and, if decreased tubulin binding provides a selective advantage, we reasoned that the TOG domain may be inactivated in some cancers. We therefore analyzed whether any reported mutations may impact TOG domain function (43, 45). Nonsense mutations that truncate the protein prior to the C-terminal kinase domain are common in MEKK1—in line with the kinase activity promoting apoptosis. Missense mutations are also prevalent across the gene, with two of the five recurrent sites found within the C-terminal portion of the TOG domain (Fig. 6*A*). Modeling the position of these sites (Arg853 and Asp806) on a putative MEKK1–tubulin complex suggests that each lies at the tubulin-binding interface (Fig. 6*B*). The nonconservative amino acid substitutions suggest a high likelihood that they would disrupt tubulin-binding function. Overall, mutations in the TOG domain of MEKK1, particularly at the tubulin-binding interface, are selectively enriched in a subset of tumor samples, suggesting they may confer a survival advantage in the context of oncogenesis.

Discussion

This work presents evidence for the presence of a previously uncharacterized domain within MEKK1, spanning residues 548 to 867 of the human protein. Based on a crystal structure and structural homology, this domain of MEKK1 was predicted to be a tubulin-binding TOG domain, which was confirmed by in vitro binding studies and mutagenesis. ITC experiments show that the MEKK1 TOG domain selectively binds the curved conformation of tubulin. The curved conformation of tubulin is associated with nonpolymerized tubulin, microtubule end structures, and microtubule catastrophes. Within cells, mutant MEKK1 that was unable to bind tubulin induces less microtubule density at the leading edge of polarized cells. Collectively, these results suggest that the MEKK1 TOG shares some features of canonical TOG domains, but repurposes the TOG fold to function within a protein that activates signaling cascades.

TOG domains are traditionally involved in the regulation of microtubule dynamics. Current models of TOG-catalyzed tubulin polymerization all rely on the presence of multiple TOG domains in a single polypeptide or a complex (46–49). MEKK1 only contains one TOG domain, suggesting that MEKK1 is less likely to act as a microtubule polymerase, although single TOG domains can affect microtubule dynamics in some cases (34, 35). At the structural level, MEKK1 has common TOG features, but also differences at the N and C termini that may facilitate its role. One close structural homolog of MEKK1 is another recently identified TOG domain from CEP104 (*SI Appendix*, Fig. S6 and Table S3 and refs. 50 and 51). The CEP104 and MEKK1 TOG domains both share a similar pair of arginine-rich C-terminal helices relative to canonical TOGs. However, the Cep104 protein is proposed to be multimeric due to oligomerization through

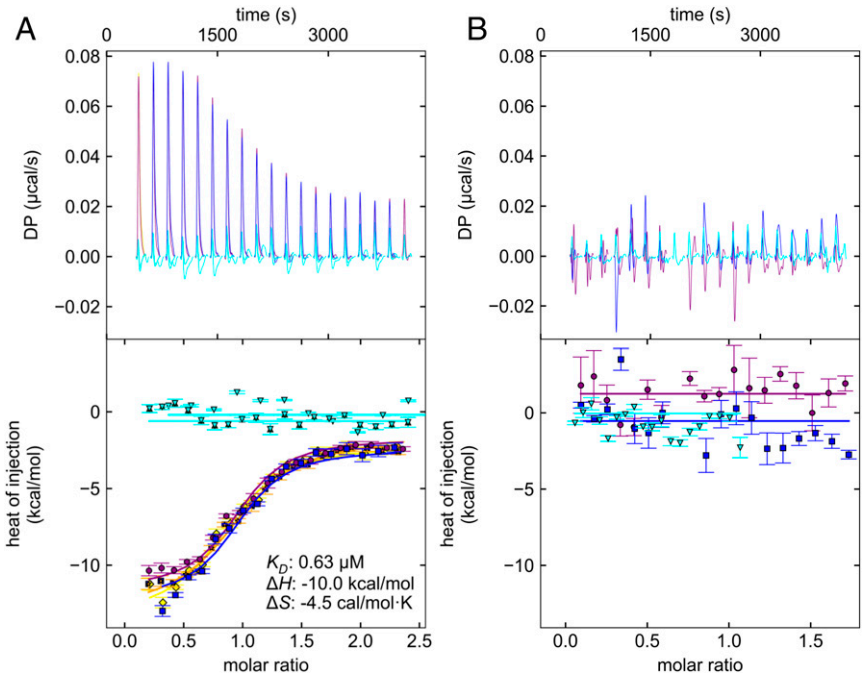

Fig. 4. ITC comparison between MEKK1 TOG interacting with the free tubulin and paclitaxel-stabilized microtubules. (*A*) Thermograms (*Top*) and fitted isotherms (*Bottom*) from a global analysis of four experiments measuring MEKK1 TOG binding to tubulin in nonpolymerizing conditions, shown in maroon, orange, yellow, and blue. MEKK1 TOG dilution experiment and tubulin dilution experiment shown in cyan. (*B*) Thermograms (*Top*) and fitted isotherms (*Bottom*) from two experiments measuring MEKK1 TOG binding to stabilized microtubules, shown in maroon, and blue. Microtubule dilution experiment is shown in cyan. DP in the shown thermograms denotes differential power measured in the ITC experiment.

an adjacent coiled-coil domain, thus enabling it to function in a similar manner to canonical TOG arrays (51). Several TOG domains are found in close proximity to a basic region that helps confer microtubule localization (52). MEKK1 contains a highly basic sequence between the SWIM and RING domains, spanning amino acids 367 to 420 with a predicted isoelectric point of 11. Although it is 120 amino acids away from the N terminus of the TOG domain, this region could confer some additional affinity to microtubules based on electrostatic interaction alone, and is worthy of future investigation.

The role of MEKK1 in mediating the cellular response to stressors that alter cell shape is well documented. MEKK1 has been found to mediate apoptosis following actin disruption, intermediate filament disruption, and microtubule disruption (23, 28), as well as cold shock and hyperosmotic stress, which both induce cytoskeletal remodeling (8, 53, 54). In terms of caspase-dependent activation of MEKK1 (22, 55–57), the presence of a TOG domain directly N-terminal to the caspase cleavage site suggests cleavage would release the kinase domain from association with tubulin. In terms of caspase-independent activation of MEKK1 (8, 23, 28), the role of tubulin binding in activation remains to be fully determined. However, because the MEKK1 TOG domain has a much higher affinity for the curved conformation of tubulin in vitro, the MEKK1 TOG domain in vivo could either predominantly bind to free (unpolymerized) tubulin or to one of several curved protofilament conformations present within the reaction cycle of tubulin (58). Such function could enable sensing the status of microtubules directly, which could bring MEKK1 to the sites of catastrophe and induce clustering of MEKK1. Further studies are required to understand how preferential binding of MEKK1 to specific states of free or partially polymerized tubulin impacts signaling function.

In unstressed cells expressing mutant MEKK1, we see a defect in the formation of microtubule networks at the leading edge. This finding suggests that MEKK1 may play a role in the cross-talk between dynamic microtubule ends and the actin cytoskeleton, given that it is apparently able to directly bind to both types of filament that are present at the leading edge (59). How MEKK1 is regulated and the specific substrates at the leading edge both remain pertinent questions. Logical candidates for interaction partners include Rho GTPases, previously shown to regulate MEKK1 and actin dynamics (59–61), and Calponin-3, a MEKK1 kinase substrate within the actin cytoskeleton known to impact cellular contractility (11).

Either direct sensing of microtubule catastrophes or involvement in cellular contractility and migration would be quite relevant to the role of MEKK1 in cancer treatment and metastasis, respectively. Somatic MEKK1 mutations have been identified as significantly enriched in cancer samples in prostate, lung, breast, and ovarian tumor samples (62). The finding that two of the most frequent missense mutations in cBioPortal occur at the tubulin-binding interface points to an important role for tubulin association in normal cellular homeostasis, which can be lost in cancer to confer a survival advantage. One possible mechanism would be mutations removing a mechanism of MEKK1 clustering at nascent curved protofilaments, which could serve as transient scaffolds for MEKK1 oligomerization and activation. Alternatively, mutations at the MEKK1-tubulin interface could remodel MEKK1's interactions with other microtubule-associated proteins during migration and metastasis, for instance, ERK1/2 (63, 64), known microtubule-associated protein kinases and confirmed downstream targets of MEKK1 (8, 65). However, the exact mechanism by which tubulin-binding mutants impact cancer progression remains to be determined.

MEKK1 is a signaling protein uniquely positioned at the crossroads between ubiquitin and phosphorylation signaling pathways (66). A direct interaction between MEKK1 and tubulin expands the repertoire of this versatile signaling protein and provides a mechanism for the sensing of microtubule status by MEKK1. Such function could affect substrate selection of MEKK1 kinase or ubiquitin ligase

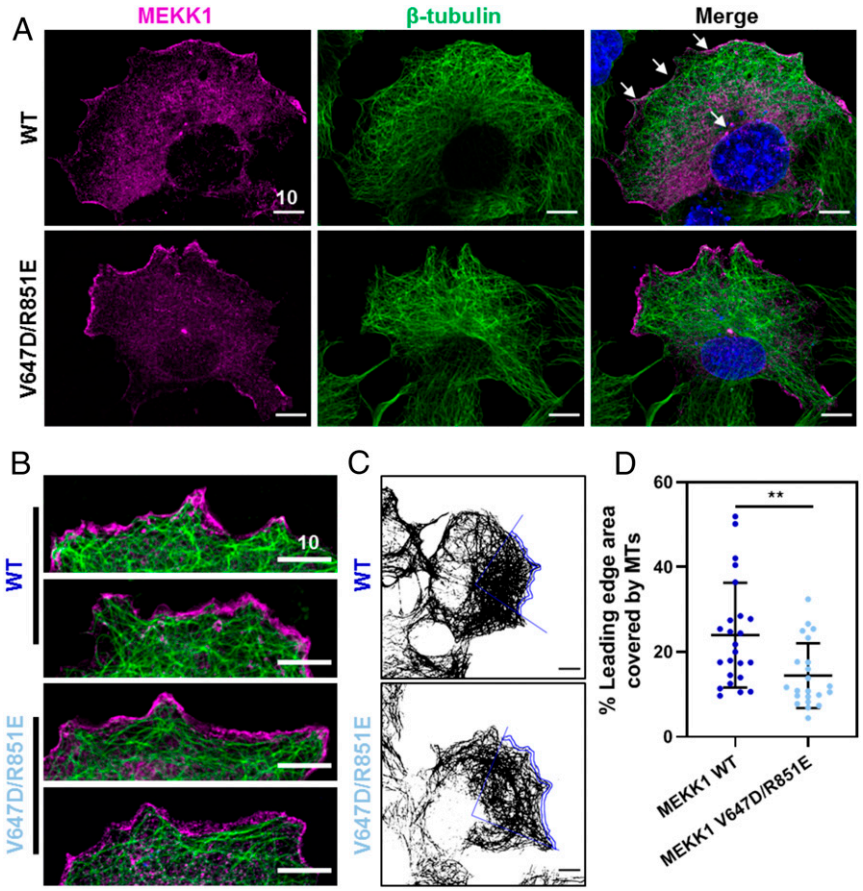

Fig. 5. Analysis of mutant MEKK1 in COS-7 cells. (*A*) Distribution of WT (*Top*) and V647D/R851E (*Bottom*) MEKK1 and tubulin in COS-7 cells. MEKK1 signal is shown as magenta, tubulin as green, and DAPI blue. The arrows indicate MEKK1 enrichment at the leading edge and at centrosomes. (*B*) A detail of the leading edge of polarized cells expressing WT MEKK1 (*Top*) and MEKK1 V647D/R851E (*Bottom*). (*C*) An illustration of the quantification of leading-edge microtubule density. (*D*) Fraction of leading-edge area covered by microtubules in WT MEKK1-expressing cells (left, dark blue) and MEKK1 V647D/R851E-expressing cells (right, light blue). $^{**}P < 0.01$. All scale bars are 10 μm.

activities and eventual cellular response. Future studies aimed at uncovering the exact mechanism by which tubulin regulates MEKK1 activity will be relevant both to understanding the role of MEKK1 in normal stress responses, and the efficacy of microtubule disrupting therapies in patients bearing MEKK1 mutations.

Materials and Methods

Sequence Analysis. Q13233 protein sequence from uniprot.org provided a reference protein sequence of MEKK1, and NM_005921.1 messenger RNA sequence from the National Center for Biotechnology Information database provided a reference nucleotide sequence of MEKK1. Sequence-based disorder prediction was carried out by PONDr VL-XT (25) using the PONDr webserver. ConSurf (67–69) provided per-residue conservation scores by search with the reference *Homo sapiens* MEKK1 sequence in ConSeq mode with default settings.

Cloning. ProteinCCD was used to aid in design of MEKK1 constructs and primers for ligation-independent cloning (70). MEKK1 542 to 888 construct (*H. sapiens* MEKK1 TOG) was amplified from the MegaMan human transcriptome library (Agilent). The TOG construct was cloned into pETNKI-his-3C-LIC-kan vector, which was a gift from Titia Sixma (Addgene #108703, Netherlands Cancer Institute, Amsterdam, Netherlands). Site-directed mutagenesis was carried out by a modified QuikChange protocol using overlapping primers with mutagenic mismatch and 3′ overhangs (71).

Protein Purification. All constructs were expressed in *E. coli* BL21(DE3) in lysogeny broth media, induced with isopropyl β-D-1-thiogalactopyranoside overnight at 18 °C, and lysed by sonication. The cell lysate was clarified by centrifugation before protein purification. After purification, all proteins were aliquoted and snap-frozen in liquid nitrogen before storing at –80 °C. Before use, snap-frozen protein aliquots were thawed at room temperature (RT) (MEKK1 constructs), or at 37 °C (tubulin and components of the ubiquitin cascade), centrifuged at 20,000 × *g* at 4 °C, and kept on ice until use.

The MEKK1 TOG domain was purified for crystallization by Ni^{2+} affinity chromatography, 3c protease cleavage, and dialysis against 300 mM NaCl, 10 mM Hepes pH 7.6, 2 mM dithiothreitol (DTT). For all other purposes, the domain was further purified by SEC in 300 mM NaCl, 10 mM Hepes pH 7.6. Tubulin was purified from fresh bovine brains using two rounds of polymerization–depolymerization in high-molarity 1,4-piperazinediethanesulfonate (PIPES) buffer (72).

Crystallization. MEKK1 TOG domain was used for crystallization trials at concentrations of 3.5 mg/mL to 30 mg/mL in HBS300 and protein:precipitant drop ratios of 33 to 90% in total volumes of 300 nL to 1,200 nL. Crystallization plates were set up using the mosquito nanoliter-pipetting system (TTP Labtech) in MRC two- or three-well crystallization plates (Swissci) using the high-throughput screens Index HT, SaltRx HT, (Hampton Research) and Morpheus HT (Molecular Dimensions). Homemade solutions for crystallization screen expansion or cryoprotection were prepared from analytical grade chemicals and filtered through a 22-μm syringe filter before use. The crystal used for native data collection was grown in 1.5 M sodium acetate and 0.1 M BIS-Tris propane pH 6.9 at a drop ratio of 4:1, and cryoprotected in 1.8 M sodium acetate, 0.1 M BIS-Tris propane pH 6.9, and 30% glycerol. The crystal used for anomalous data collection was grown in 1.6 M sodium acetate, 0.1 M BIS-Tris propane pH 7 at a drop ratio of 9:1, and soaked for 30 s in cryoprotectant consisting of 1.8 M sodium acetate, 0.1 M BIS-Tris propane pH 6.9, 30% glycerol, and 500 mM sodium iodide before freezing.

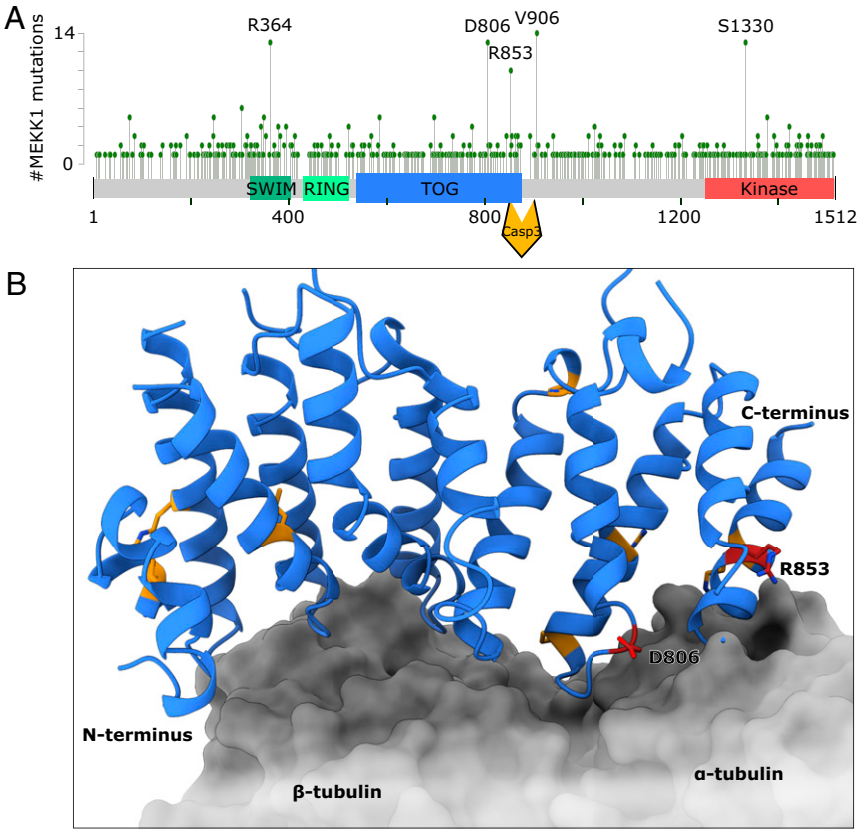

Fig. 6. MEKK1 TOG domain harbors mutations in human cancers. (*A*) Missense mutations in MEKK1 in a curated set of nonredundant human cancer sequence dataset. The TOG domain contains two of the top five mutation hot spots in the MEKK1 sequence. (*B*) A model of MEKK1 TOG–tubulin interaction, with MEKK1 TOG domain residues mutated three or more times colored orange and residues mutated 10 or more times colored red. Asp-806 and Arg-853 both lay on the interface with α-tubulin.

Data Collection and Structure Solution. X-ray diffraction data collection was performed at the Australian Synchrotron using the MX-1 beamline and ADSC Quantum 210r detector (73). The native dataset was collected at a wavelength of 0.9537 Å, and the anomalous dataset was collected at a wavelength of 1.4586 Å.

Raw data were processed with XDS (74), the space group was determined with Pointless (75, 76), and the dataset was scaled with Aimless (77). The aimless package also utilizes Ctruncate, Mtzdump, Unique, Freerflag, and Cad programs of the ccp4 suite to output the scaled dataset (78). The structure was solved using Auto-Rickshaw's single isomorphous replacement with anomalous scattering pipeline (79).

Refinement. The initial model was rebuilt and refined using ARP/wARP (80, 81), followed by iterative manual model modification and refinement using coot (82), phenix (83), and refmac (84). After initial refinement against the dataset truncated at 2.1-Å resolution with R_{work}/R_{free} values of 0.2053/0.2338, the initial dataset was reprocessed with XDS to a resolution of 1.9 Å, including weak high-resolution reflections displaying statistically significant CC1/2. The model refined against the 2.1-Å data was then used for automated building using phenix.autobuild with the 1.9 Å data. Subsequent refinement using coot and phenix.refine yielded a fully refined structure with R_{work}/R_{free} of 0.2071/0.2297. A simple composite omit map was generated using phenix.composite_omit_map. Structural biology applications used in refinement were compiled and configured by SBGrid (92). The diffraction data and refined structure coordinates were deposited in the Protein Data Bank (PDB) under PDB ID code 6WHB.

SEC. In coelution assays, purified MEKK1 constructs were mixed with tubulin in a 2 to 3:1 molar ratio. DTT was added to a concentration of 1 mM. Then 100 μL to 500 μL of the protein mixture were injected on Superdex 200 Increase column equilibrated in 300 mM NaCl and 10 mM Hepes pH 7.6, connected to an ÄKTA pure fast protein liquid chromatography system (both GE Healthcare); 250-μL fractions were collected and analyzed on sodium dodecyl sulfate polyacrylamide gel electrophoresis (SDS/PAGE). In coelution assay with colchicine, tubulin was preincubated with 1 mM colchicine at 0 °C for 20 min prior to size exclusion, and the size-exclusion buffer contained 20 μM colchicine.

MALLS. MALLS data were collected using a Wyatt Dawn 8+ detector (Wyatt Technology) and Waters 410 differential refractometer (Waters) in line with an ÄKTA pure chromatography system fitted with a Superdex 200 Increase column (both GE Healthcare). Data were analyzed using ASTRA 5.3.4 software (Wyatt Technology).

Model Preparation. Structural overlays were prepared using secondary structure matching in coot and MatchMaker in UCSF ChimeraX (26). Source coordinates' PDB codes are stated in the respective figure legends.

ITC. A low-volume Affinity ITC instrument controlled by ITCRun software was used to collect ITC data (both TA instruments). Four hundred microliters of TOG domain at 13.42 mg/mL were desalted into 250 mM NaCl, 250 μM TCEP, and 20 mM sodium phosphate at pH 6.5 (ITC buffer) using a 5-mL HiTrap Desalting column (GE Healthcare). Likewise, 80 μL of tubulin at 10.9 mg/mL were desalted into the same buffer. The top fractions from each desalting run were collected, their concentration was determined, and both were degassed at 40 kPa at 25 °C for 10 min.

One hundred millimolar GTP in water was diluted with ITC buffer to a concentration of 1 mM, and 1 μL/100 μL of tubulin was added for a concentration of 10 μM in cell. The sample cell was loaded with 350 μL of tubulin/GTP solution, and the ITC syringe was loaded with 320 μL of TOG solution. An ITC run consisted of 1 injection of 0.5 μL, followed by 19 injections of 2.5 μL at 30 °C with a stirring rate of 75 rpm with automatic equilibration set for collection of data with small heats. For each replicate run, tubulin was prepared fresh in the same manner.

For TOG dilution control, tubulin was substituted for the buffer supplemented with GTP as described above. For tubulin dilution control, the TOG solution was substituted with buffer. The collected data were exported to .xml format using NanoAnalyze (TA Instruments), the baselines were determined using NITPIC, and the thermodynamic parameters of the interaction were determined in a global analysis using SEDPHAT (85, 86). The data were

plotted using GUSSI (85). The blank runs were not subtracted from any of the interaction runs but were plotted alongside the interaction thermograms and isotherms instead.

To probe the interaction between stable microtubules and MEKK1 TOG, stable microtubules were prepared, and their buffer was exchanged by two rounds of centrifugation at 20,800 × *g* for 20 min and resuspension of the microtubule pellet in ITC buffer. All other actions were done exactly as in the case of probing soluble tubulin–MEKK1 TOG interaction.

Stable Microtubule Preparation. Stable microtubules were prepared using paclitaxel stabilization (87). An aliquot of tubulin at 4 mg/mL to 10 mg/mL was thawed and mixed with an equal volume of prewarmed 2 × Pol buffer (80 mM PIPES-K pH 6.8, 16% dimethyl sulfoxide (DMSO), 3 mM $MgCl_2$, 1 mM EGTA, 2.5 mM GTP), and the mixture was incubated at 37 °C for 10 min. Paclitaxel (LC Labs) was then added stepwise: 1 μL of 100 μM paclitaxel in 5% DMSO was added at the 10- and 15-min marks, and 1 μL of 2 mM paclitaxel in 100% DMSO was added at the 20- and 25-min marks. Then 8 μL of 2 mM paclitaxel in 100% DMSO was added at the 30-min mark, and the microtubules were left to polymerize at 37 °C for another 3 h. The polymerized microtubules were then transferred to RT and left to stabilize for at least 16 h prior to use. Their concentration was determined by diluting them 10-fold in 5 mM $CaCl_2$ in 80 mM PIPES-K pH 6.8, 1 mM $MgCl_2$, 1 mM ethylene glycol-bis(β-aminoethyl ether)-N,N,N′,N′-tetraacetic acid (Brinkley resuspension buffer with 80 mM PIPES, BRB80), leaving them to depolymerize for at least 30 min on ice, measuring A280, and calculating concentration with $\varepsilon = 115{,}000$ and M = 110 kDa.

Cosedimentation Assay. The stabilized microtubules were separated from smaller species by centrifugation for 20 min at 20,800 × *g* at 20 °C, and the pellets were resuspended in BRB80 + 20% glycerol; 250 μL of BRB80 supplemented with 20% glycerol was added to Eppendorf tubes, a 2:1 molar mixture of TOG and microtubules was layered on top of the glycerol solution, and the samples were centrifuged at 20,800 × *g* for 40 min at RT. The top 20 μL were aspirated as the top fraction, the middle 230 μL were discarded as the intermediate fraction, 20 μL of 2 × SDS/PAGE buffer was added to the bottom 20 μL, and the pellet was resuspended. The contents of the top and bottom fractions were analyzed using SDS/PAGE.

NS-EM. The 300-mesh in-house carbon-coated copper grids were glow discharged using BioRad E5100 scanning electron microscopy coating system modified in-house for glow discharging grids (BioRad Microscience Ltd.) in low vacuum (<200 Pa) with a current of 15 mA for 60 s.

The 0.9 mg/mL paclitaxel-stabilized microtubules were mixed with MEKK1 TOG at 5.5 mg/mL, incubated at RT for 30 min, and centrifuged at 20,800 × *g* for 20 min at RT. The supernatant was discarded, and the pellet was resuspended in 300 mM NaCl in 10 mM Hepes pH 7.6 and immediately placed on grids and stained; 4 μL of the solution were applied onto the grids, most of the protein solution was blotted away with Whatman No.1 filter paper, and the grids were washed twice using deionized water and stained using 1% Uranyl acetate at pH 4.5. After 1 min, the excess stain was blotted off, and the grids were air dried. Dried grids were stored, until imaging, at RT. Grids were imaged on Philips CM-100 BioTWIN transmission electron microscope with a LaB_6 electron source at 100 kV (Philips/FEI Corporation), fitted with a MegaViewIII digital camera (Olympus Soft Imaging Solutions GmbH). The iTEM imaging platform (EMSIS GmbH) was used to record micrographs.

Cryo-EM. MEKK1 TOG–microtubule protein solution was prepared exactly as in the case of NS-EM; 2.5 μL of the solution was applied on glow-discharged C-flat grids (Protochips), and the grids were blotted and frozen with KF80 specimen plunge-freezing device (Leica) or Vitrobot Mark IV (Thermo Fisher Scientific).

Data collection on frozen-hydrated specimens was carried out using JEOL JEM-2200FS with omega energy filter in cryo configuration with Gatan 914 High-tilt tomography holder and cryotransfer system, fitted with DE-20 4k × 5k direct detector with 6.4 μm × 6.4 μm pixels (Direct Electron). The microscope was operated at 200 kV accelerating voltage with a field emission gun with ZrO/W Schottky emitter. An in-column omega filter with a slit width of 20 eV was used when recording micrographs. The JEOL TEM Controller Application was used for microscope control, and SerialEM was used for semiautomated data collection. Twenty-frame movies were collected at a dose rate of ∼1e-/Å2/frame at a magnification of 30,000×, corresponding to a pixel size of 2 Å. Movie stacks were aligned and dose-weighted using the camera manufacturer's alignment scripts. Aligned, dose-weighted micrographs were imported to RELION 2 or 3 (88, 89). The contrast transfer function (CTF) was estimated using gctf (90). The CTF fit for each micrograph was examined, and poor fits were excluded from further processing. Straight microtubules were manually picked in RELION, avoiding bends, breaks, and contamination. Microtubule helix particles were extracted as overlapping 400 × 400-pixel particles, offset by 40 pixels along the central axis of the helix. The 2D classification of the extracted particles was performed in RELION, ignoring the CTF until first peak due to the extremely strong structural features of the microtubule lattice distorting the low-resolution CTF signature.

Mammalian Cell Culture. COS-7 cell line was cultured in Dulbecco's modified Eagle's medium containing 10% fetal calf serum under standard tissue culture conditions (5% CO_2, 20% O_2). All lines were authenticated by short tandem repeat polymorphism, single-nucleotide polymorphism, and fingerprint analyses; COS-7 cells were seeded in 35-mm imaging dishes coated with 0.08 mg/mL collagen at a density of 2×10^5 cells per dish. Twenty-four hours after seeding, cells were transfected with 1.5 μg of either MEKK1-V5 or MEKK1 V647D/R851E-V5 using Jet Prime transfection reagent. Twenty-four hours after transfection, cell monolayers were scored as in a standard wound healing assay, washed with complete medium, and incubated at 37 °C for 5 h. Samples were fixed for 20 min with ice-cold methanol and stored overnight in phosphate-buffered saline (PBS) at 4 °C. Samples were then blocked in 2% bovine serum albumin/PBS for 30 min at RT, incubated with rabbit monoclonal anti-V5 tag (CST #13202, 1:500 dilution) and mouse monoclonal anti-β-tubulin (Santa Cruz #sc-58880, 1:200 dilution) primary antibodies for 1 h at RT, washed twice in blocking solution, incubated with goat-anti-rabbit IgG AlexaFluor 488 and goat-anti-mouse IgG AlexaFluor 647 (Jackson ImmunoResearch #111-545-008 and #115-605-166, both 1:250 dilution) secondary antibodies for 30 min at RT, washed twice with PBS, counterstained with DAPI for 5 min at RT, and washed twice with PBS. Images were collected with a Leica SP8 scanning confocal microscope using a 63×/1.4 NA objective.

Images of cells displaying a clear polarized morphology were analyzed with ImageJ software. A 90° angle was positioned at the centrosome to define the region of the leading edge that would be analyzed. The leading edge was manually demarcated using the MEKK1 signal, and a 15-pixel ROI was defined from this line. The coverage of microtubules within this ROI was calculated using an automatic threshold. Once all data were collected, the average threshold was calculated from all WT and MEKK1 images, and all images were reanalyzed using this value. Results were plotted as the percentage of leading-edge area containing microtubule signal. The results were checked for correlation between the size of ROI and percentage of leading-edge area covered by microtubules. In addition, the relative, single-cell expression levels of MEKK1 WT and MEKK1 V647D/R851E were also measured by high-content imaging. This was performed using identical transfection conditions, and imaged on the Thermo-Scientific Cellomics Arrayscan VTI platform, as previously described (91). For both imaging analyses, a Mann–Whitney test was used to determine statistical significance.

Data Availability. The diffraction data and refined structure coordinates were deposited in the PDB under PDB ID code 6WHB. All study data are included in the article and *SI Appendix*.

ACKNOWLEDGMENTS. This work was supported by Rutherford Discovery Fellowship from the New Zealand government administered by the Royal Society of New Zealand, held by P.D.M., and a University of Otago Doctoral Scholarship, held by P.F. We also thank the New Zealand synchrotron group for facilitating access to the macromolecular crystallography beamlines at the Australian Synchrotron, as well as the beamline staff of the Australian Synchrotron, particularly Daniel Erikson for anomalous phasing data collection strategies. We thank Mihnea Bostina and Richard Easingwood from the Otago Micro and Nanoscale Imaging Unit, and Rui Zhang (Washington University in St. Louis) and Carolyn Moores (Birkbeck, University of London) for helpful discussions regarding EM, tubulin preparation, and data processing.

1. W. Peti, R. Page, Molecular basis of MAP kinase regulation. *Protein Sci.* **22**, 1698–1710 (2013).
2. Y. Kondo *et al*., Cryo-EM structure of a dimeric B-Raf:14-3-3 complex reveals asymmetry in the active sites of B-Raf kinases. *Science* **366**, 109–115 (2019).
3. D. Matallanas *et al*., Raf family kinases: Old dogs have learned new tricks. *Genes Cancer* **2**, 232–260 (2011).
4. E. Park *et al*., Architecture of autoinhibited and active BRAF-MEK1-14-3-3 complexes. *Nature* **575**, 545–550 (2019).
5. F. S. Lee, J. Hagler, Z. J. Chen, T. Maniatis, Activation of the IkappaB alpha kinase complex by MEKK1, a kinase of the JNK pathway. *Cell* **88**, 213–222 (1997).
6. F. S. Lee, R. T. Peters, L. C. Dang, T. Maniatis, MEKK1 activates both IkappaB kinase α and IkappaB kinase β. *Proc. Natl. Acad. Sci. U.S.A.* **95**, 9319–9324 (1998).

7. Y. Xia, Z. Wu, B. Su, B. Murray, M. Karin, JNKK1 organizes a MAP kinase module through specific and sequential interactions with upstream and downstream components mediated by its amino-terminal extension. *Genes Dev.* **12**, 3369–3381 (1998).
8. T. Yujiri, S. Sather, G. R. Fanger, G. L. Johnson, Role of MEKK1 in cell survival and activation of JNK and ERK pathways defined by targeted gene disruption. *Science* **282**, 1911–1914 (1998).
9. J. C. Deak, D. J. Templeton, Regulation of the activity of MEK kinase 1 (MEKK1) by autophosphorylation within the kinase activation domain. *Biochem. J.* **322**, 185–192 (1997).
10. S. Xu *et al*., Cloning of rat MEK kinase 1 cDNA reveals an endogenous membrane-associated 195-kDa protein with a large regulatory domain. *Proc. Natl. Acad. Sci. U.S.A.* **93**, 5291–5295 (1996).
11. H. Hirata *et al*., MEKK1-dependent phosphorylation of calponin-3 tunes cell contractility. *J. Cell Sci.* **129**, 3574–3582 (2016).
12. J. A. Witowsky, G. L. Johnson, Ubiquitylation of MEKK1 inhibits its phosphorylation of MKK1 and MKK4 and activation of the ERK1/2 and JNK pathways. *J. Biol. Chem.* **278**, 1403–1406 (2003).
13. A. Matsuzawa *et al*., Essential cytoplasmic translocation of a cytokine receptor-assembled signaling complex. *Science* **321**, 663–668 (2008).
14. N. Charlaftis *et al*., The MEKK1 PHD ubiquitinates TAB1 to activate MAPKs in response to cytokines. *EMBO J.* **33**, 2581–2596 (2014).
15. Z. Lu, S. Xu, C. Joazeiro, M. H. Cobb, T. Hunter, The PHD domain of MEKK1 acts as an E3 ubiquitin ligase and mediates ubiquitination and degradation of ERK1/2. *Mol. Cell* **9**, 945–956 (2002).
16. M. A. Rieger *et al*., The MEKK1 SWIM domain is a novel substrate receptor for c-Jun ubiquitylation. *Biochem. J.* **445**, 431–439 (2012).
17. Y. Xia *et al*., MEKK1 mediates the ubiquitination and degradation of c-Jun in response to osmotic stress. *Mol. Cell. Biol.* **27**, 510–517 (2007).
18. E. Steed *et al*., MarvelD3 couples tight junctions to the MEKK1-JNK pathway to regulate cell behavior and survival. *J. Cell Biol.* **204**, 821–838 (2014).
19. L. B. Christerson, C. A. Vanderbilt, M. H. Cobb, MEKK1 interacts with alpha-actinin and localizes to stress fibers and focal adhesions. *Cell Motil. Cytoskeleton* **43**, 186–198 (1999).
20. E. Gallagher *et al*., Kinase MEKK1 is required for CD40-dependent activation of the kinases Jnk and p38, germinal center formation, B cell proliferation and antibody production. *Nat. Immunol.* **8**, 57–63 (2007).
21. L. Aravind, L. M. Iyer, E. V. Koonin, Scores of RINGS but no PHDs in ubiquitin signaling. *Cell Cycle* **2**, 123–126 (2003).
22. C. Widmann, P. Gerwins, N. L. Johnson, M. B. Jarpe, G. L. Johnson, MEK kinase 1, a substrate for DEVD-directed caspases, is involved in genotoxin-induced apoptosis. *Mol. Cell. Biol.* **18**, 2416–2429 (1998).
23. E. Tricker *et al*., Apoptosis induced by cytoskeletal disruption requires distinct domains of MEKK1. *PLoS One* **6**, e17310 (2011).
24. T. K. Schlesinger *et al*., Apoptosis stimulated by the 91-kDa caspase cleavage MEKK1 fragment requires translocation to soluble cellular compartments. *J. Biol. Chem.* **277**, 10283–10291 (2002).
25. P. Romero *et al*., Sequence complexity of disordered protein. *Proteins* **42**, 38–48 (2001).
26. E. Krissinel, K. Henrick, Secondary-structure matching (SSM), a new tool for fast protein structure alignment in three dimensions. *Acta Crystallogr. D Biol. Crystallogr.* **60**, 2256–2268 (2004).
27. S. Gibson, C. Widmann, G. L. Johnson, Differential involvement of MEK kinase 1 (MEKK1) in the induction of apoptosis in response to microtubule-targeted drugs versus DNA damaging agents. *J. Biol. Chem.* **274**, 10916–10922 (1999).
28. R. Kwan, J. Burnside, T. Kurosaki, G. Cheng, MEKK1 is essential for DT40 cell apoptosis in response to microtubule disruption. *Mol. Cell. Biol.* **21**, 7183–7190 (2001).
29. T. Yujiri *et al*., MEK kinase 1 (MEKK1) transduces c-Jun NH2-terminal kinase activation in response to changes in the microtubule cytoskeleton. *J. Biol. Chem.* **274**, 12605–12610 (1999).
30. P. Ayaz, X. Ye, P. Huddleston, C. A. Brautigam, L. M. Rice, A TOG: αβ-tubulin complex structure reveals conformation-based mechanisms for a microtubule polymerase. *Science* **337**, 857–860 (2012).
31. A. E. Byrnes, K. C. Slep, TOG-tubulin binding specificity promotes microtubule dynamics and mitotic spindle formation. *J. Cell Biol.* **216**, 1641–1657 (2017).
32. J. C. Fox, A. E. Howard, J. D. Currie, S. L. Rogers, K. C. Slep, The XMAP215 family drives microtubule polymerization using a structurally diverse TOG array. *Mol. Biol. Cell* **25**, 2375–2392 (2014).
33. T. Maki, A. D. Grimaldi, S. Fuchigami, I. Kaverina, I. Hayashi, CLASP2 has two distinct TOG domains that contribute differently to microtubule dynamics. *J. Mol. Biol.* **427**, 2379–2395 (2015).
34. A. Aher *et al*., CLASP suppresses microtubule catastrophes through a single TOG domain. *Dev. Cell* **46**, 40–58.e8 (2018).
35. S. Majumdar *et al*., An isolated CLASP TOG domain suppresses microtubule catastrophe and promotes rescue. *Mol. Biol. Cell* **29**, 1359–1375 (2018).
36. E. H. Kellogg *et al*., Insights into the distinct mechanisms of action of taxane and non-taxane microtubule stabilizers from cryo-EM structures. *J. Mol. Biol.* **429**, 633–646 (2017).
37. E. Nogales, S. G. Wolf, K. H. Downing, Structure of the α β tubulin dimer by electron crystallography. *Nature* **391**, 199–203 (1998).
38. M. T. Hsu, M. Bonomi, D. A. Agard, M. P. Jacobson, L. X. Peng, The free energy profile of tubulin straight-bent conformational changes, with implications for microtubule assembly and drug discovery. *PLoS Comput. Biol.* **10**, e1003464 (2014).
39. S. Banerjee, G. Chakrabarti, B. Bhattacharyya, Colchicine binding to tubulin monomers: A mechanistic study. *Biochemistry* **36**, 5600–5606 (1997).
40. R. B. G. Ravelli *et al*., Insight into tubulin regulation from a complex with colchicine and a stathmin-like domain. *Nature* **428**, 198–202 (2004).
41. A. Nawrotek, M. Knossow, B. Gigant, The determinants that govern microtubule assembly from the atomic structure of GTP-tubulin. *J. Mol. Biol.* **412**, 35–42 (2011).
42. L. Pecqueur *et al*., A designed ankyrin repeat protein selected to bind to tubulin caps the microtubule plus end. *Proc. Natl. Acad. Sci. U.S.A.* **109**, 12011–12016 (2012).
43. E. Cerami *et al*., The cBio cancer genomics portal: An open platform for exploring multidimensional cancer genomics data. *Cancer Discov.* **2**, 401–404 (2012).
44. D. F. Easton *et al*.; SEARCH collaborators; kConFab; AOCS Management Group, Genome-wide association study identifies novel breast cancer susceptibility loci. *Nature* **447**, 1087–1093 (2007).
45. J. Gao *et al*., Integrative analysis of complex cancer genomics and clinical profiles using the cBioPortal. *Sci. Signal.* **6**, pl1 (2013).
46. P. Ayaz *et al*., A tethered delivery mechanism explains the catalytic action of a microtubule polymerase. *eLife* **3**, e03069 (2014).
47. E. A. Geyer, M. P. Miller, C. A. Brautigam, S. Biggins, L. M. Rice, Design principles of a microtubule polymerase. *eLife* **7**, e34574 (2018).
48. S. Nithianantham *et al*., Structural basis of tubulin recruitment and assembly by microtubule polymerases with tumor overexpressed gene (TOG) domain arrays. *eLife* **7**, e38922 (2018).
49. K. C. Slep, R. D. Vale, Structural basis of microtubule plus end tracking by XMAP215, CLIP-170, and EB1. *Mol. Cell* **27**, 976–991 (2007).
50. C. Al-Jassar *et al*., The ciliopathy-associated Cep104 protein interacts with tubulin and Nek1 kinase. *Structure* **25**, 146–156 (2017).
51. L. Rezabkova, S. H. W. Kraatz, A. Akhmanova, M. O. Steinmetz, R. A. Kammerer, Biophysical and structural characterization of the centriolar protein Cep104 interaction network. *J. Biol. Chem.* **291**, 18496–18504 (2016).
52. P. O. Widlund *et al*., XMAP215 polymerase activity is built by combining multiple tubulin-binding TOG domains and a basic lattice-binding region. *Proc. Natl. Acad. Sci. U.S.A.* **108**, 2741–2746 (2011).
53. S. Breton, D. Brown, Cold-induced microtubule disruption and relocalization of membrane proteins in kidney epithelial cells. *J. Am. Soc. Nephrol.* **9**, 155–166 (1998).
54. P. Nunes *et al*., Hypertonic stress promotes autophagy and microtubule-dependent autophagosomal clusters. *Autophagy* **9**, 550–567 (2013).
55. M. H. Cardone, G. S. Salvesen, C. Widmann, G. Johnson, S. M. Frisch, The regulation of anoikis: MEKK-1 activation requires cleavage by caspases. *Cell* **90**, 315–323 (1997).
56. J. C. Deak *et al*., Fas-induced proteolytic activation and intracellular redistribution of the stress-signaling kinase MEKK1. *Proc. Natl. Acad. Sci. U.S.A.* **95**, 5595–5600 (1998).
57. S.-G. Shiah, S.-E. Chuang, M.-L. Kuo, Involvement of Asp-Glu-Val-Asp-directed, caspase-mediated mitogen-activated protein kinase kinase 1 Cleavage, c-Jun N-terminal kinase activation, and subsequent Bcl-2 phosphorylation for paclitaxel-induced apoptosis in HL-60 cells. *Mol. Pharmacol.* **59**, 254–262 (2001).
58. G. J. Brouhard, L. M. Rice, Microtubule dynamics: An interplay of biochemistry and mechanics. *Nat. Rev. Mol. Cell Biol.* **19**, 451–463 (2018).
59. M. Dogterom, G. H. Koenderink, Actin-microtubule crosstalk in cell biology. *Nat. Rev. Mol. Cell Biol.* **20**, 38–54 (2019).
60. E. D. Gallagher, S. Gutowski, P. C. Sternweis, M. H. Cobb, RhoA binds to the amino terminus of MEKK1 and regulates its kinase activity. *J. Biol. Chem.* **279**, 1872–1877 (2004).
61. L. B. Christerson *et al*., p115 Rho GTPase activating protein interacts with MEKK1. *J. Cell. Physiol.* **192**, 200–208 (2002).
62. Z. Kan *et al*., Diverse somatic mutation patterns and pathway alterations in human cancers. *Nature* **466**, 869–873 (2010).
63. R. E. Harrison, E. A. Turley, Active erk regulates microtubule stability in H-ras-transformed cells. *Neoplasia* **3**, 385–394 (2001).
64. J. W. Haycock, N. G. Ahn, M. H. Cobb, E. G. Krebs, ERK1 and ERK2, two microtubule-associated protein 2 kinases, mediate the phosphorylation of tyrosine hydroxylase at serine-31 in situ. *Proc. Natl. Acad. Sci. U.S.A.* **89**, 2365–2369 (1992).
65. M. Karandikar, S. Xu, M. H. Cobb, MEKK1 binds raf-1 and the ERK2 cascade components. *J. Biol. Chem.* **275**, 40120–40127 (2000).
66. P. Filipčík, J. R. Curry, P. D. Mace, When worlds collide—Mechanisms at the interface between phosphorylation and ubiquitination. *J. Mol. Biol.* **429**, 1097–1113 (2017).
67. H. Ashkenazy, E. Erez, E. Martz, T. Pupko, N. Ben-Tal, ConSurf 2010: Calculating evolutionary conservation in sequence and structure of proteins and nucleic acids. *Nucleic Acids Res.* **38**, W529–W533 (2010).
68. G. Celniker *et al*., ConSurf: Using evolutionary data to raise testable hypotheses about protein function. *Isr. J. Chem.* **53**, 199–206 (2013).
69. M. Landau *et al*., ConSurf 2005: The projection of evolutionary conservation scores of residues on protein structures. *Nucleic Acids Res.* **33**, W299–W302 (2005).
70. W. T. M. Mooij, E. Mitsiki, A. Perrakis, C. C. D. Protein, ProteinCCD: Enabling the design of protein truncation constructs for expression and crystallization experiments. *Nucleic Acids Res.* **37**, W402–W405 (2009).
71. H. Liu, J. H. Naismith, An efficient one-step site-directed deletion, insertion, single and multiple-site plasmid mutagenesis protocol. *BMC Biotechnol.* **8**, 91 (2008).
72. M. Castoldi, A. V. Popov, Purification of brain tubulin through two cycles of polymerization-depolymerization in a high-molarity buffer. *Protein Expr. Purif.* **32**, 83–88 (2003).
73. N. P. Cowieson *et al*., MX1: A bending-magnet crystallography beamline serving both chemical and macromolecular crystallography communities at the Australian synchrotron. *J. Synchrotron Radiat.* **22**, 187–190 (2015).
74. W. Kabsch, XDS. *Acta Crystallogr. D Biol. Crystallogr.* **66**, 125–132 (2010).
75. P. Evans, Scaling and assessment of data quality. *Acta Crystallogr. D Biol. Crystallogr.* **62**, 72–82 (2006).
76. P. R. Evans, An introduction to data reduction: Space-group determination, scaling and intensity statistics. *Acta Crystallogr. D Biol. Crystallogr.* **67**, 282–292 (2011).

77. P. R. Evans, G. N. Murshudov, How good are my data and what is the resolution? *Acta Crystallogr. D Biol. Crystallogr.* **69**, 1204–1214 (2013).
78. M. D. Winn *et al*., Overview of the CCP4 suite and current developments. *Acta Crystallogr. D Biol. Crystallogr.* **67**, 235–242 (2011).
79. S. Panjikar, V. Parthasarathy, V. S. Lamzin, M. S. Weiss, P. A. Tucker, Auto-rickshaw: An automated crystal structure determination platform as an efficient tool for the validation of an X-ray diffraction experiment. *Acta Crystallogr. D Biol. Crystallogr.* **61**, 449–457 (2005).
80. G. Langer, S. X. Cohen, V. S. Lamzin, A. Perrakis, Automated macromolecular model building for X-ray crystallography using ARP/wARP version 7. *Nat. Protoc.* **3**, 1171–1179 (2008).
81. R. J. Morris *et al*., Breaking good resolutions with ARP/wARP. *J. Synchrotron Radiat.* **11**, 56–59 (2004).
82. P. Emsley, K. Cowtan, Coot: Model-building tools for molecular graphics. *Acta Crystallogr. D Biol. Crystallogr.* **60**, 2126–2132 (2004).
83. P. D. Adams *et al*., The Phenix software for automated determination of macromolecular structures. *Methods* **55**, 94–106 (2011).
84. G. N. Murshudov *et al*., REFMAC5 for the refinement of macromolecular crystal structures. *Acta Crystallogr. D Biol. Crystallogr.* **67**, 355–367 (2011).
85. C. A. Brautigam, H. Zhao, C. Vargas, S. Keller, P. Schuck, Integration and global analysis of isothermal titration calorimetry data for studying macromolecular interactions. *Nat. Protoc.* **11**, 882–894 (2016).
86. H. Zhao, G. Piszczek, P. Schuck, SEDPHAT–A platform for global ITC analysis and global multi-method analysis of molecular interactions. *Methods* **76**, 137–148 (2015).
87. C. Moores, Studying microtubules by electron microscopy. *Methods Cell Biol.* **88**, 299–317 (2008).
88. S. He, S. H. W. Scheres, Helical reconstruction in RELION. *J. Struct. Biol.* **198**, 163–176 (2017).
89. J. Zivanov *et al*., New tools for automated high-resolution cryo-EM structure determination in RELION-3. *eLife* **7**, 1–38 (2018).
90. K. Zhang, Gctf: Real-time CTF determination and correction. *J. Struct. Biol.* **193**, 1–12 (2016).
91. S. P. Kennedy *et al*., Targeting promiscuous heterodimerization overcomes innate resistance to ERBB2 dimerization inhibitors in breast cancer. *Breast Cancer Res.* **21**, 43 (2019).
92. A. Morin *et al*., Collaboration gets the most out of software. *eLife* **2**, e01456 (2013).